Multi-Parameter Analysis and Measurement of Resonances in Grid-Connected Converters with LCL Filters

Dominik Schulz, Andreas Liske, Marc Hiller
Karlsruhe Institute of Technology (KIT)
Institute of Electrical Engineering (ETI)
Kaiserstraße 12, Karlsruhe, Germany
Tel.: +49 721 608 46528
E-Mail: dominik.schulz@kit.edu

URL: http://eti.kit.edu

Index Terms—≪LCL≫, ≪converter control≫, ≪active damping≫, ≪impedance analysis≫, ≪experimental testing≫

Abstract—**LCL filters offer high attenuation of grid current ripple, but are challenging from a control perspective due to the resonant peak in their transfer function. The influence of selected individual parameters has already been the studied in several papers. This paper builds on this existing body of work and provides a more comprehensive analysis of all relevant variables influencing the resonance. In addition, dependencies between the parameters are explored. Stability and resonances are evaluated using frequency responses and an impedance based approach. Finally, the analysis results are confirmed with measurements.**

I. INTRODUCTION

As the share of regenerative and decentralized power generation rises in the electrical grid, the interfacing grid converter turns into a central and critical device. An important requirement for the deployed converter systems is the attenuation of the switching harmonics caused by the pulse-width modulation (PWM). Compared to more simple inductive L-type filters, LCL filters offer a higher attenuation rate of -60 dB/dec above the resonant frequency, resulting in higher possible control dynamics [1]. On the other hand, the higher order of the LCL filter also makes it prone to resonances. Some form of damping is therefore required to mitigate the risk of

oscillations. The simplest solution is to insert damping resistors in series with the filter capacitors. While this passive damping offers low complexity and guaranteed damping performance, it also increases system losses and leads to a reduced attenuation of the LCL filter [2]. Active damping (AD) approaches are preferable, since they replace the damping resistors with adapted control methods. The various AD approaches described in the literature can be broadly categorized as filter-based or state-feedback-based [3], [4]. While filter-based methods require no additional sensors or complexity in the form of state estimators, these approaches exhibit more sensitivity to parameter uncertainties [5].

One source of instability is the resonant peak caused by the LCL filter in the current control loop. It can therefore be considered as internal to the system. A second source of instability is the interaction of the converter with the grid impedance or neighboring converter systems [4], together with the feedback loop created by a voltage feed-forward path in the control [6], [7]. To ensure external stability, two main approaches are used in the literature. The state space modelling of multiple converters and non-ideal grids is the more general method. It can reveal all possible system resonances and instabilities as eigenvalues of the state matrix, but requires detailed knowledge of all involved participants and elements [8]. In contrast, the impedance-based stability analysis [9] does not demand an accurate knowledge of internal device parameters [10]. Instead, it can be utilized with black-box measurements of both grid and converter impedances using well-known frequency domain stability criteria.

This paper does not focus on the individual methods to achieve sufficient damping of the LCL filter resonance

already presented in the literature [3]–[5], [11], [12]. Instead, it systematically examines numerous variables that contribute to the occurrence of a resonance at a specific frequency, including multiple control parameters, the selected feedback current and the grid impedance. In this manner, the aim of this paper is to identify the impact of the aforementioned variables and their interdependencies, while keeping the system and all other parameters constant. In contrast to the literature listed above, the investigation in the present paper is carried out using a two-level converter based on SiC-MOSFETs with a higher switching and sampling frequency of $50\,\text{kHz}$, together with an LCL filter with a resonant frequency of $6\,\text{kHz}$. The investigation is conducted using two analytical methods. The first is the frequency response of the open loop transfer function, the second is the impedance model mentioned above. The results of this analytical investigation are then confirmed by hardware measurements, in which all the parameters considered are modified both independently and concurrently.

II. MODELLING OF SYSTEM RESONANCES AND INFLUENCING VARIABLES

This chapter presents the system under study, focusing on the control structure which contains multiple parameters relevant to the resulting system resonances. Additionally, two modelling methods are described to consider both internal and external stability.

A. System Description

Fig. 1 shows the general structure of the converter system analyzed in this paper. The three-phase voltage source inverter is assumed to be supplied with a constant DC voltage v_{DC} and is connected to the grid using an LCL filter. The converter output voltage v_{i} results in converter-side currents denoted as i_{i}. This current is divided into a current i_{c} flowing into the capacitor branch and the remaining current i_{g} flowing into the point of common coupling (PCC). The voltage at the PCC v_{PCC} is not identical to the ideal grid line voltage v_{g}, as they are separated by the grid impedance Z_{g}. The measured system quantities i_{i}, i_{g} and v_{PCC} are inputs to the converter control. The current controller determines new output voltages, which are translated into switching patterns by the pulse-width modulator.

The control structure is shown in detail in Fig. 2, where the parameters that influence the resonance considered in this paper are highlighted with green numbering:

1) The choice of the feedback current: Since both the grid-side current i_{g} and the converter-side current
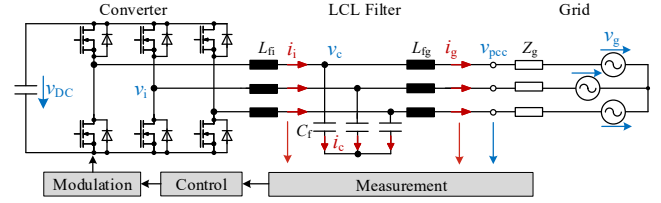

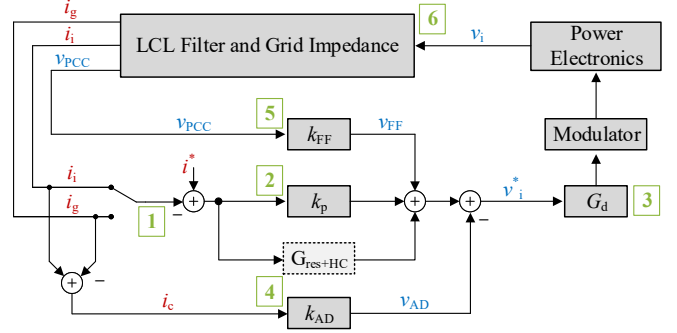Fig. 1: System structure with measured quantities

Fig. 2: Control structure with potential resonance sources

i_{i} are available as measured values, the control can be a set to track either of those currents.
2) The proportional controller gain k_{p}: This gain translates the current error into the output voltage setpoint v_{i}^{*}. In the utilized PR controller, additional resonant elements provide high controller gains around the fundamental and harmonic frequencies. As these resonant paths only operate at their specified frequencies below the investigated resonances, they can be neglected in this paper.
3) The signal delay shown as transfer function G_{d}: It is caused by the measurement delay, computation time of the control and the dead time introduced by the PWM modulation. Its effect can be demonstrated by artificially increasing the signal delay.
4) The active damping gain k_{AD}: The capacitor currents are calculated by taking the difference between the measured inverter currents i_{i} and grid-side currents i_{g}. They are then multiplied by the active damping gain k_{AD} for state-feedback active damping, which implements a virtual capacitor series resistance.
5) The feed-forward gain k_{FF}: If chosen, the measured line voltages at the PCC v_{PCC} can be fed forward to the controller output by selecting $k_{\text{FF}} = 1$.
6) The grid impedance connecting the PCC to the grid voltage v_{g}: This impedance determines how the measured currents and the voltage at the PCC
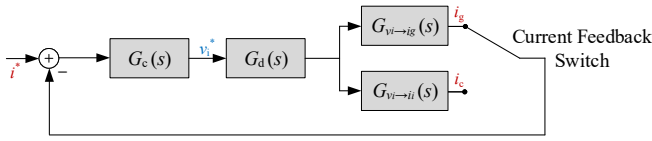
Fig. 3: System transfer functions for internal stability

Fig. 4: Signal flow graph including the effect of the PCC voltage
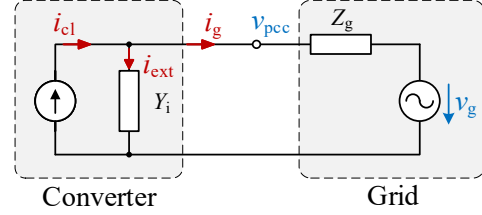
Fig. 5: Impedance model of converter-grid system

are influenced by the converter output voltage v_i.

B. Internal Stability

Internal stability refers to the stability of the converter and filter system without considering the external grid impedance. In the following, only the small-signal behaviour will be considered, so that the system can be assumed to be linear around its operating point. This allows the application of the well-established Nyquist stability criterion of the closed loop system with the frequency response of the open loop transfer function.

The derivation of the open loop transfer function is shown in Fig. 3. Since only the proportional controller path is considered, the controller transfer function simplifies to $G_\mathrm{c}(s) = k_\mathrm{p}$. The delay can be modelled as $G_\mathrm{d}(s) = e^{-T_\mathrm{d}s}$ with $T_\mathrm{d} = \frac{n_\mathrm{del}}{f_\mathrm{sw}}$ as the time delay consists of n_del sampling period multiples. Transfer functions from the converter output voltage v_i to the inverter-side current i_i and the grid-side current i_g can be found in the relevant literature [4] and are not derived here. The resulting open loop transfer functions are

$$
\begin{aligned}
G_{\mathrm{ol},i_i}(s) &= G_\mathrm{c}(s) \cdot G_\mathrm{d}(s) \cdot G_{v_i \to i_i}(s) \\
&= k_\mathrm{p} e^{-T_\mathrm{d}s} \frac{1 + s^2 L_\mathrm{fg} C_\mathrm{f}}{s^3 L_\mathrm{fi} L_\mathrm{fg} C_\mathrm{f} + s(L_\mathrm{fi} + L_\mathrm{fg})} \\
&= k_\mathrm{p} e^{-T_\mathrm{d}s} \frac{1}{s L_\mathrm{fi}} \frac{s^2 + \omega_{LC}^2}{s^2 + \omega_{LCL}^2}
\end{aligned}
\tag{1}
$$

and

$$
\begin{aligned}
G_{\mathrm{ol},i_g}(s) &= G_\mathrm{c}(s) \cdot G_\mathrm{d}(s) \cdot G_{v_i \to i_g}(s) \\
&= k_\mathrm{p} e^{-T_\mathrm{d}s} \frac{1}{s^3 L_\mathrm{fi} L_\mathrm{fg} C_\mathrm{f} + s(L_\mathrm{fi} + L_\mathrm{fg})} \\
&= k_\mathrm{p} e^{-T_\mathrm{d}s} \frac{1}{s L_\mathrm{fi}} \frac{\omega_{LC}^2}{s^2 + \omega_{LCL}^2},
\end{aligned}
\tag{2}
$$

with the LCL resonant frequency ω_{LCL} and the grid-side LC resonant frequency ω_{LC} defined as

$$
\omega_{LCL} = \sqrt{\frac{L_\mathrm{fi} + L_\mathrm{fg}}{L_\mathrm{fi} L_\mathrm{fg} C_\mathrm{f}}} \quad \text{and} \quad \omega_{LC} = \frac{1}{\sqrt{L_\mathrm{fg} C_\mathrm{f}}}.
\tag{3}
$$

The Bode plots of the open loop transfer function can be interpreted according to the Nyquist criterion in order to provide information on critical resonant frequencies and stability margins.
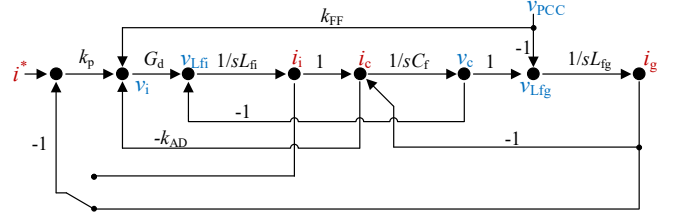
C. External Stability

External stability considerations are required when the effects of the grid impedance or interactions between neighboring converters cannot be neglected. In the control structure presented in Fig. 2, the feedback loop closed by the PCC voltage feed-forward is not taken into account in the transfer functions shown in Fig. 3. It therefore requires a more comprehensive analysis. Fig. 4 shows the signal flow graph for the extended system including interactions with the PCC voltage v_PCC. The two considered external variables considered in this work are the grid impedance Z_g and the choice of PCC voltage feed-forward k_FF.

The chosen approach to describe the interaction between the converter system and the external elements is to model both as impedances [9]. The converter is represented by a current source with a current of $i_\mathrm{cl} = G_{\mathrm{cl},i} i^*$ that results from the closed-loop current transfer function $G_{\mathrm{cl},i}$, in parallel with a frequency-dependent admittance Y_i. The grid is modelled as an ideal voltage source with voltage v_g and a series impedance Z_g. The grid current i_g consists of the internally controlled component and the current resulting from an external change in v_PCC:

$$
i_\mathrm{g} = i_\mathrm{cl} - i_\mathrm{ext} = G_{\mathrm{cl},i} i^* - v_\mathrm{PCC} Y_\mathrm{i}
\tag{4}
$$

The PCC voltage v_PCC can then be described as

$$
v_\mathrm{PCC} = (v_\mathrm{g} + Z_\mathrm{g} G_{\mathrm{cl},i} i^*) \frac{1}{1 + Z_\mathrm{g} Y_\mathrm{i}}.
\tag{5}
$$

This equation includes the influence of the grid voltage and grid impedance. It is assumed that the three-phase

system is symmetrical and there is no cross-coupling, so the system can be represented as a single phase [13]. Slower PLL and DC link dynamics are neglected in this paper. The external stability can then be assessed by considering the open-loop transfer function T, which is given by the ratio of the converter and grid impedance $T = Z_g Y_i = Z_g / Z_i$. Thus, the critical points of T are those where $|Z_g| \geq |Z_i|$ and $\angle Z_g - \angle Z_i = (2n + 1)\pi$ with $n \in \mathbb{Z}$ applies.

To describe the converter admittance, the signal flow graph in Fig. 4 is used to determine transfer functions from the PCC voltage v_{PCC} to the grid-side current i_g using Mason's gain formula [14]:

$$Y_{i_i} = \frac{-i_g(s)}{v_{\text{PCC}}(s)} = \tag{6}$$

$$\frac{s^2 L_{\text{fi}} C_{\text{f}} + s C_{\text{f}} (k_{\text{p}} + k_{\text{AD}}) G_{\text{d}} - k_{\text{FF}} G_{\text{d}} + 1}{s^3 L_{\text{fi}} L_{\text{fg}} C_{\text{f}} + s^2 L_{\text{fg}} C_{\text{f}} (k_{\text{p}} + k_{\text{AD}}) G_{\text{d}} + s(L_{\text{fi}} + L_{\text{fg}}) + k_{\text{p}} G_{\text{d}}}$$

$$Y_{i_g} = \frac{-i_g(s)}{v_{\text{PCC}}(s)} = \tag{7}$$

$$\frac{s^2 L_{\text{fi}} C_{\text{f}} + s C_{\text{f}} k_{\text{AD}} G_{\text{d}} - k_{\text{FF}} G_{\text{d}} + 1}{s^3 L_{\text{fi}} L_{\text{fg}} C_{\text{f}} + s^2 L_{\text{fg}} C_{\text{f}} k_{\text{AD}} G_{\text{d}} + s(L_{\text{fi}} + L_{\text{fg}}) + k_{\text{p}} G_{\text{d}}}$$

In order to ensure overall stability, the examination of external stability presupposes internal stability, i.e. the stability of $G_{\text{cl},i}$. The external stability is therefore not sufficient, but necessary for complete system stability. This will be neglected for the following impedance-based considerations, since the aim is to identify possible sources of instability and not to guarantee overall stability.

III. ANALYTICAL INVESTIGATION OF INFLUENCING VARIABLES

In this section, the principal parameters influencing the resonances of the converter and filter system are investigated analytically. The more straightforward transfer function model given in (1) and (2) is used to analyze the influence of the feedback current selection, the controller gain k_{p} and the signal delay n_{del} on the internal stability. The converter impedance will be used to examine the effect of the active damping, voltage feed-forward and grid impedance variations on the external stability. Given the number of influencing parameters, it is not possible to describe all possible mutual dependencies in this paper. Instead, only the most relevant interdependencies are presented.

The relevant system parameters are listed in Table I. For the single-loop transfer functions, the grid inductance of $L_g = 50\,\mu\text{H}$ can be added to the grid-side filter

TABLE I: Relevant system parameters

Parameter	Symbol	Value
Converter-side LCL inductance	L_{fi}	$100\,\mu\text{H}$
Grid-side LCL inductance	L_{fg}	$50\,\mu\text{H}$
LCL filter capacitance	C_{f}	$14.1\,\mu\text{F}$
Switching and sampling frequency	f_{sw}	$50\,\text{kHz}$
DC link voltage	v_{DC}	$600\,\text{V}$
LCL resonant frequency ($L_g = 50\,\mu\text{H}$)	ω_{LCL}	$5.99\,\text{kHz}$
LC resonant frequency ($L_g = 50\,\mu\text{H}$)	ω_{LC}	$4.24\,\text{kHz}$

TABLE II: Default control and grid parameters

i	k_{p}	n_{del}	k_{AD}	k_{FF}	L_g
i_g	2.5	2.5	0	0	$50\,\mu\text{H}$

inductance. This results in the specified LCL and LC resonant frequencies ω_{LCL} and ω_{LC}. Unless otherwise specified, the default parameters given in Table II are assumed, while one parameter is varied to investigate its influence. The time delay of $T_{\text{d}} = \frac{n_{\text{del}}}{f_{\text{sw}}} = 2.5\,T_{\text{sw}}$ consists of a control computation delay of one sampling step, one half time step due to the modulation and an additional sampling step that is caused by the external grid-side current measurement.

A. Current Feedback Selection

The selection of the current to be controlled is decisive for the resulting resonances. This is evident from the transfer functions given in (1) and (2). The resulting transfer functions are shown in Fig. 6. The LCL resonant frequency $f_{LCL} = 6\,\text{kHz}$ and the grid-side LC resonant frequency $f_{LC} = 4.2\,\text{kHz}$ are visible. When the inverter-side current is used, a double zero occurs at f_{LC} in the transfer function G_{ol,i_i} given in (1). The magnitude $|G|$ of the transfer function is therefore well below $0\,\text{dB}$ around f_{LC}. In this case, the crossing of $-180°$ at the LCL resonant frequency is the critical point leading to a resonance. For grid-current feedback, the phase is already below the critical value of $-180°$ at the LCL resonant frequency with the combination of signal delay, resonance and switching frequency considered. Any resulting system resonant frequency therefore lies below f_{LCL}. In the case shown, the magnitude is already above $0\,\text{dB}$ when the phase reaches $-180°$ at $f = 5\,\text{kHz}$, leading to a resonance around this frequency.

B. Controller Gain

The effect of the controller gain k_{p} on the transfer function in the case of grid-side current feedback is shown in Fig. 7. As the phase is unaffected by the controller gain, the frequency at which the magnitude $|G|$
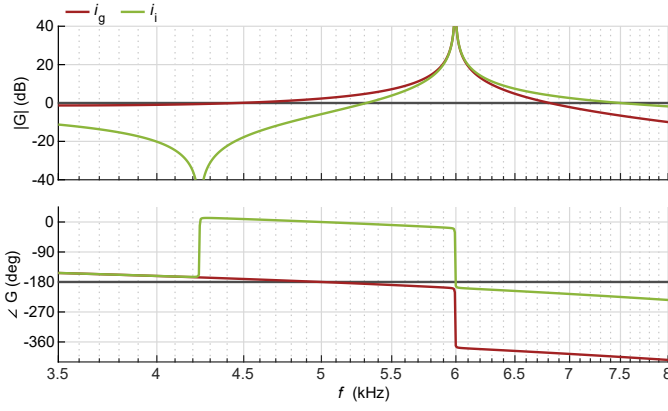
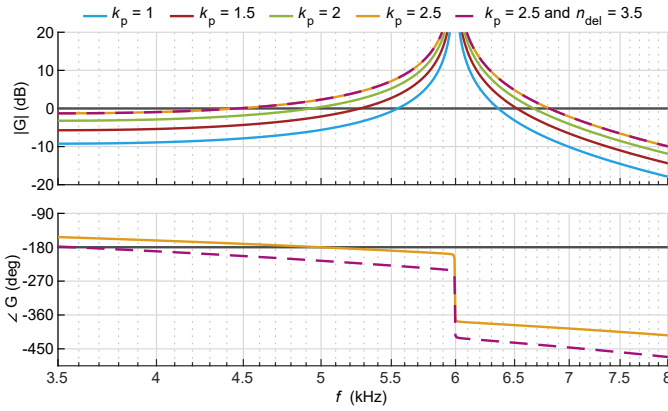Fig. 6: Transfer functions for inverter current i_i and grid current i_g

Fig. 7: Transfer functions of grid-side current i_g with variation of proportional controller gain k_p and delay steps n_{del}

reaches $0\,\text{dB}$ identifies the resonant frequency and stability. In the given case, the resonant frequency increases for higher controller gains and the system becomes unstable for $k_p \geq 2$.

C. Signal Delay

The signal delay is determined by the sampling frequency f_s and the number of sampling periods n_{del} before the measured current results in a new converter output voltage. In Fig. 7, the effect of one additional sampling period in the signal path is visible. At $f = 5\,\text{kHz}$, where the transfer function without additional delay indicates a resonance for $k_p = 2.5$, the phase shift due to this additional delay is $\Delta\varphi = \frac{5\,\text{kHz}}{50\,\text{kHz}}360° = 36°$. This phase shift causes the phase to reach $-180°$ at a lower frequency of $f = 3.8\,\text{kHz}$. As the magnitude of the transfer function is lower at this frequency, it also results in a more damped resonance, consistent with the results reported in [11].
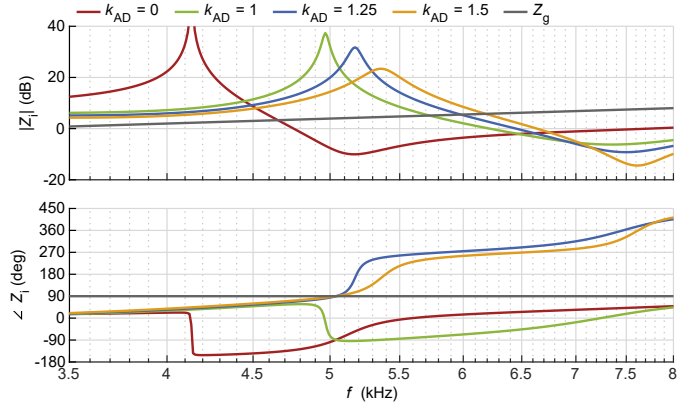

Fig. 8: Converter impedances Z_i with variation of k_{AD}

D. State-Feedback Active Damping

The effect of the active damping gain k_{AD} using the measured capacitor current is analyzed using the impedance model of the converter and filter system. The single-loop transfer function presented in section II-B does not include the active damping loop and therefore cannot provide statements regarding its influence on any resonance. In Fig. 8 the converter impedance $Z_i = 1/Y_i$ is plotted with a variation of the active damping gain k_{AD}, together with the grid impedance Z_g.

As described in section II-C, the stability assessment using the converter impedance is based on the ratio of the impedances $T = Z_g/Z_i$ as the open loop transfer function. The grid impedance Z_g is assumed to be purely inductive, so $\angle Z_g = 90°$. The converter impedance $|Z_i|$ for with $k_{AD} = 0$ crosses $|Z_g|$ at $4.7\,\text{kHz}$, while $\angle Z_i$ rises above $-90°$ at a higher frequencies. Hence, $\angle T$ crosses $180°$ while $|T| > 1$, implying an unstable resonance. For $k_{AD} = 1$, $|Z_g|$ crosses $|Z_i|$ while $\angle Z_i$ is already above $-90°$. This indicates that the active damping is able to stabilize the system.

With $k_{AD} \geq 1.25$, the poles of the converter impedance given in (7) move to the right half plane (RHP). This is visible as the $180°$ phase jump at the resonant frequency is no longer negative but positive, which also explains the difference of $360°$ at the final frequency. This double RHP pole in Z_i results in a double RHP zero in T. For $k_{AD} = 1.25$, the system is marginally stable, with the phase $\angle Z_i = 270°$ and the magnitude $|Z_i| = |Z_g|$ at $6\,\text{kHz}$. Further increasing k_{AD} destabilizes the system with critical frequencies above $6\,\text{kHz}$. A more intuitive explanation for this effect is that the subtraction of the capacitor current i_c effectively shifts the feedback current from i_g to i_i.
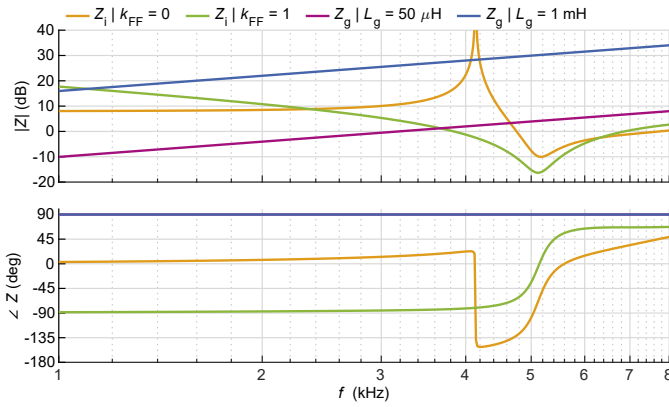
Fig. 9: Converter impedances Z_i with variation of k_{FF} and grid impedance Z_g at low and high inductance

E. Feed-Forward Control

The impact of the feed-forward gain k_{FF} is examined using the converter impedance. Its effect is only relevant when a significant grid impedance is present and the PCC voltage is affected by the converter currents. This grid impedance is not included in the internal stability analysis using the single-loop transfer functions presented in section II-B. Fig. 9 shows the converter impedance using grid-side current feedback with both enabled and disabled PCC voltage feed-forward, together with two possible grid impedances. To illustrate the effect of the enabled feed-forward path, the grid impedance with lower inductance $L_g = 50\,\mu H$ plotted in violet is considered. The phase of the converter impedance without feed-forward is plotted in yellow and crosses $-90°$ at $5\,kHz$ while the magnitude of the impedance is less than that of the grid impedance. This implies unstable system behaviour with a resonance around this frequency. The converter impedance with feed-forward is plotted in green and is close to $-90°$ when its magnitude falls below that of the grid impedance at $3.6\,kHz$. This indicates stability, albeit with low attenuation.

F. Grid Impedance

The variation of the unknown grid impedance is a major concern for the control of LCL filters as it leads to a shifting resonant frequency ω_{LCL}. In general, any change of the grid impedance Z_g naturally affects the impedance ratio T and thus entails the possibility of a resulting external instability. As described in the previous section III-E, the converter impedance is affected by the selection of the feed-forward gain k_{FF}. While this may not be a problem for lower grid impedances, the resulting ratio between the converter impedance and an increased grid impedance can lead to instability. This is visible in

Fig. 9, which shows the impedance of the converter with enabled feed-forward control $k_{FF} = 1$ plotted in green, together with a variation of the grid impedance. For a strong grid with a low grid inductance of $L_g = 50\,\mu H$ plotted in violet, $|T|$ crosses $0\,dB$ at $3.6\,kHz$ with a phase reserve of approximately $10°$. For a weaker grid with a higher grid inductance of $1\,mH$ plotted in blue, the crossing point of $|T|$ is shifted to $1.1\,kHz$ and the phase reserve is reduced to almost zero.

IV. Experimental Results

In this chapter, the analytical considerations of the previous part are complemented by measurements that confirm the conclusions of the two modelling methods used.

A. Hardware Description

The power electronic hardware together with the signal processing unit used for the measurements is shown in Fig. 10a and presented in detail in [15]. It is equipped with SiC MOSFETs and contains sensors for the converter current i_i and the voltage at the PCC v_{PCC}. The signal processing board with an Artix™-7 FPGA, which is mounted at the front side, implements the control shown in Fig. 2. The grid-side current i_g is measured using external sensors that require an additional sampling period, so $n_{del} = 2.5$.

All investigated control parameters can be tuned online to directly observe their effects, without the need to shut down the system and reprogram the FPGA. In addition, an extra delay of one control time step to be inserted into the signal path and the selection of the current measurement to be used for the control can be configured using a transmitted control bit field. For all measurements with PCC voltage feed-forward disabled, the resonant paths tuned to the harmonic frequencies indicated in Fig. 2 are active to minimize the effect of grid voltage distortions. All measurements are performed with a reactive current setpoint of $i_g^* = 10\,A$. The LCL filter is shown in Fig. 10b. It is placed on the bottom of the switching cabinet, above a second LCL filter used for an IGBT-based converter. The LCL filter contains no additional damping resistances, but the non-ideal nature of both the filter inductors and capacitors results in small parasitic resistances. Since no resistances are included in the model, the measurements are expected to show more damped resonances.

B. Variation of Investigated Parameters

Table III lists all the measurement configurations carried out, together with the resulting resonant frequency

(a) Power converter with mounted control unit [15]
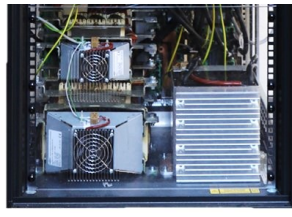
(b) LCL filter within switching cabinet

Fig. 10: Hardware used for measurements

TABLE III: Measured resonant frequencies

i	k_{p}	n_{del}	k_{AD}	k_{FF}	L_{g}	f_{res}	Figs.
i_{g}	2.5	2.5	0	0	50 μH	4.6 kHz	11,12,13,14
i_{i}	2.5	2.5	0	0	50 μH	7.4 kHz	11
i_{g}	1	2.5	0	0	50 μH	–	12
i_{g}	2	2.5	0	0	50 μH	4.9 kHz	12
i_{g}	2.5	3.5	0	0	50 μH	–	12
i_{g}	2.5	2.5	1	0	50 μH	–	13
i_{g}	2.5	2.5	2	0	50 μH	7.5 kHz	13
i_{g}	2.5	2.5	2.5	0	50 μH	7.8 kHz	13
i_{g}	2.5	2.5	0	1	50 μH	3.3 kHz	14
i_{g}	2.5	2.5	0	0	1 mH	–	14
i_{g}	2.5	2.5	0	1	1 mH	1.5 kHz	14

f_{res} measured in the grid-side current i_{g}. The resonant frequency is determined by selecting the peak in the frequency spectrum if such peak is discernible.

In Fig. 11, measurements with feedback of the grid-side and converter-side currents i_{g} and i_{i} are shown. The parameters for these measurements are given in the first two rows of Table III. The frequency spectrum shows that when switching to the converter-side current i_{i}, the resonant frequency is shifted from $4.8\,\mathrm{kHz}$ to $7.2\,\mathrm{kHz}$. This is consistent with the analysis described in section III-A.

Fig. 12a shows measurements for a variation of the controller gain k_{p} and signal delay n_{del}. The corresponding entries in Table III are those in the first row and in the second block. As k_{p} increases, the resonant frequency decreases, while the amplitude of the resonance rises. Inserting one additional delay period effectively dampens
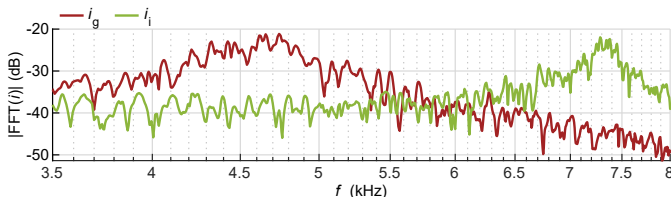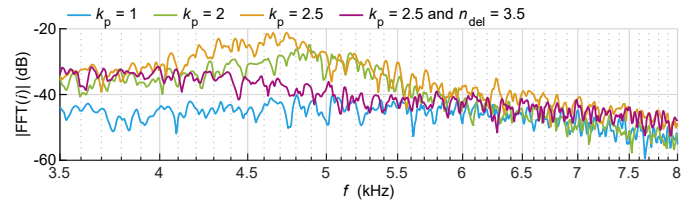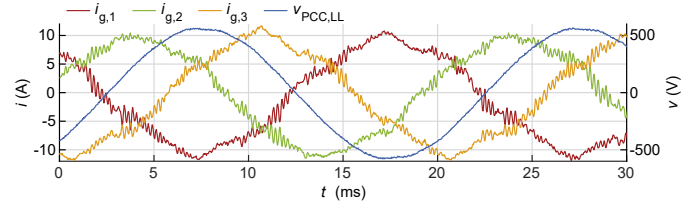

Fig. 11: FFT of i_{g} with feedback of i_{g} and i_{i}

(a) FFT of grid current i_{g} with variation of k_{p} and n_{del}

(b) Measurement of grid currents and voltage with $k_{\mathrm{p}} = 2.5$ and $n_{\mathrm{del}} = 2.5$

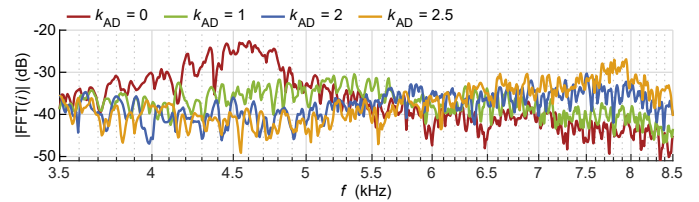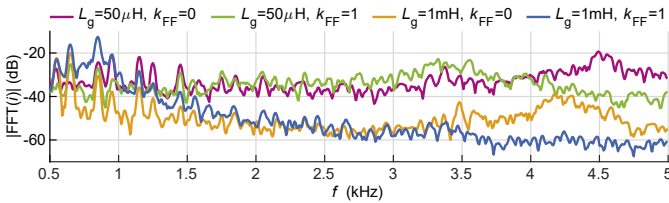Fig. 12: Measurements with variation of k_{p} and n_{del}

Fig. 13: FFT of i_{g} with $k_{\mathrm{p}} = 2.5$ and variation of k_{AD}

the resonance even for $k_{\mathrm{p}} = 2.5$. Both results are in accordance with the statements of the transfer function analysis in sections III-B and III-C. Measurements of grid currents with the observed resonance for $k_{\mathrm{p}} = 2.5$ and $n_{\mathrm{del}} = 2.5$ are shown in Fig. 12b. With the PCC voltage feed-forward disabled, the distorted grid voltage results in visible lower frequency harmonics, although these are significantly reduced by the harmonic compensators described in section II-A.

In Fig. 13, the influence of the active damping gain k_{AD} is demonstrated. For $k_{\mathrm{p}} = 2.5$, a resonance is visible at $4.5\,\mathrm{kHz}$ without active damping, which is effectively damped with $k_{\mathrm{AD}} = 1$. For higher values of k_{AD}, another resonance appears at higher frequencies, confirming the analysis in section III-D.

The effect of an enabled PCC voltage feed-forward is visible in Fig. 14a. For a strong grid with $L_{\mathrm{g}} = 50\,\mathrm{μH}$, the resonant frequency shifts from $4.6\,\mathrm{kHz}$ in the violet plot to $3.3\,\mathrm{kHz}$ in the green plot when activating the feed-forward with a slight reduction in magnitude of $3\,\mathrm{dB}$. Measurements with $k_{\mathrm{FF}} = 1$ are shown in Fig. 14b. Both the improved rejection of grid harmonics and the high frequency resonance are visible.
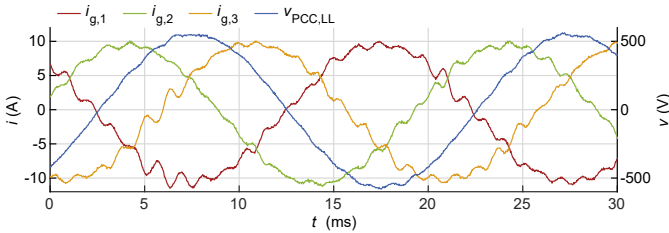
In order to measure the influence of a variation

(a) FFT of grid current i_g with variation of k_FF and L_g
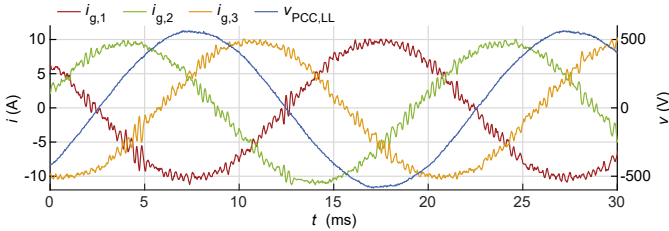
(b) Measurement of grid currents and voltage with $k_\mathrm{FF} = 1$ and $L_\mathrm{g} = 50\,\mu\mathrm{H}$

(c) Measurement of grid currents and voltage with $k_\mathrm{FF} = 1$ and $L_\mathrm{g} = 1\,\mathrm{mH}$

Fig. 14: Measurements with variation of k_FF and L_g

in the grid impedance, a $1\,\mathrm{mH}$ inductor was inserted at the grid connection point. The resulting measured frequency spectra are plotted in Fig. 14a. In the case of enabled PCC voltage feed-forward, plotted in blue, the destabilizing effect in the lower frequency range is evident, amplified by higher peaks at the harmonics of the grid frequency. This is in agreement with the analysis in section III-F. A small deviation in the resonant frequency is explained by the reduced model accuracy in the low frequency range, e.g. PLL and DC link dynamics not included in the model. With disabled feed-forward, plotted in yellow, oscillations in the low frequency range are avoided. Instead, a lower resonant peak now appears at $4.3\,\mathrm{kHz}$ as predicted by the analysis. Time-domain measurements with enabled feed-forward are shown in Fig. 14c, where the resonance is also visible in the PCC voltage v_PCC.

V. CONCLUSION

This paper systematically investigates the effect of multiple typical parameters in LCL-filtered grid converters on the resulting resonances. Where possible,

the resonances are analyzed utilizing transfer functions. For the more complex cases involving active damping using the capacitor current, PCC voltage feed-forward and a variation of the grid impedance, the analysis is carried out by modelling the converter impedance. In both cases, the influence of individual parameters on the resonant frequency and possible instabilities is illustrated. Measurements with variations of all parameters considered confirm the statements of both analytical methods. Consequently, the effects of a wide range of influencing variables and their interactions are successfully identified.

REFERENCES

[1] M. Liserre, F. Blaabjerg, and S. Hansen, "Design and Control of an LCL-Filter-Based Three-Phase Active Rectifier," *IEEE Transactions on Industry Applications*, vol. 41, no. 5, pp. 1281–1291, Sep. 2005.

[2] R. Teodorescu, M. Liserre, and P. Rodríguez, *Grid Converters for Photovoltaic and Wind Power Systems*. Wiley, 2011.

[3] J. Dannehl, F. W. Fuchs, S. Hansen, and P. B. Thøgersen, "Investigation of Active Damping Approaches for PI-Based Current Control of Grid-Connected Pulse Width Modulation Converters With LCL Filters," *IEEE Transactions on Industry Applications*, vol. 46, no. 4, pp. 1509–1517, Jul. 2010.

[4] Y. Han, M. Yang, H. Li, P. Yang, L. Xu, E. A. A. Coelho, and J. M. Guerrero, "Modeling and Stability Analysis of LCL - Type Grid-Connected Inverters: A Comprehensive Overview," *IEEE Access*, vol. 7, pp. 114 975–115 001, 2019.

[5] W. Yao, Y. Yang, X. Zhang, F. Blaabjerg, and P. C. Loh, "Design and Analysis of Robust Active Damping for LCL Filters Using Digital Notch Filters," *IEEE Transactions on Power Electronics*, vol. 32, no. 3, pp. 2360–2375, Mar. 2017.

[6] T. Messo, R. Luhtala, A. Aapro, and T. Roinila, "Accurate Impedance Model of Grid-Connected Inverter for Small-Signal Stability Assessment in High-Impedance Grids," in *2018 International Power Electronics Conference (IPEC-Niigata 2018 -ECCE Asia)*. Niigata: IEEE, May 2018, pp. 3156–3163.

[7] J. Xu, S. Xie, B. Zhang, and Q. Qian, "Robust Grid Current Control With Impedance-Phase Shaping for LCL-Filtered Inverters in Weak and Distorted Grid," *IEEE Transactions on Power Electronics*, vol. 33, no. 12, pp. 10 240–10 250, Dec. 2018.

[8] X. Wang and F. Blaabjerg, "Harmonic Stability in Power Electronic-Based Power Systems: Concept, Modeling, and Analysis," *IEEE Transactions on Smart Grid*, vol. 10, no. 3, pp. 2858–2870, May 2019.

[9] J. Sun, "Impedance-Based Stability Criterion for Grid-Connected Inverters," *IEEE Transactions on Power Electronics*, vol. 26, no. 11, pp. 3075–3078, Nov. 2011.

[10] X. Wang, F. Blaabjerg, and W. Wu, "Modeling and Analysis of Harmonic Stability in an AC Power-Electronics-Based Power System," *IEEE Transactions on Power Electronics*, vol. 29, no. 12, pp. 6421–6432, Dec. 2014.

[11] J. Wang, J. D. Yan, L. Jiang, and J. Zou, "Delay-Dependent Stability of Single-Loop Controlled Grid-Connected Inverters with LCL Filters," *IEEE Transactions on Power Electronics*, vol. 31, no. 1, pp. 743–757, Jan. 2016.

[12] S. G. Parker, B. P. McGrath, and D. G. Holmes, "Regions of Active Damping Control for LCL Filters," *IEEE Transactions on Industry Applications*, vol. 50, no. 1, pp. 424–432, Jan. 2014.

[13] X. Wang, L. Harnefors, and F. Blaabjerg, "Unified Impedance Model of Grid-Connected Voltage-Source Converters," *IEEE Transactions on Power Electronics*, vol. 33, no. 2, pp. 1775–1787, Feb. 2018.

[14] S. J. Mason, "Feedback Theory-Further Properties of Signal Flow Graphs," *Proceedings of the IRE*, vol. 44, no. 7, pp. 920–926, Jul. 1956.

[15] R. Schwendemann, S. Decker, M. Hiller, and M. Braun, "A Modular Converter- and Signal-Processing-Platform for Academic Research in the Field of Power Electronics," in *2018 International Power Electronics Conference (IPEC-Niigata 2018 -ECCE Asia)*, May 2018, pp. 3074–3080.